

## High-temperature Fischer-Tropsch synthesis over FeTi mixed oxide model catalysts: Tailoring activity and stability by varying the Ti/Fe ratio

Santos, Vera P.; Borgers, Liam; Sartipi, Sina; van der Linden, Bart; Dugulan, Iulian; Chojecki, A; Davidian, T; Ruitenbeek, M; Meima, GR; Kapteijn, Freek

**DOI**

[10.1016/j.apcata.2017.01.002](https://doi.org/10.1016/j.apcata.2017.01.002)

**Publication date**

2017

**Document Version**

Accepted author manuscript

**Published in**

Applied Catalysis A: General

**Citation (APA)**

Santos, V. P., Borgers, L., Sartipi, S., van der Linden, B., Dugulan, I., Chojecki, A., Davidian, T., Ruitenbeek, M., Meima, GR., Kapteijn, F., Makkee, M., & Gascon, J. (2017). High-temperature Fischer-Tropsch synthesis over FeTi mixed oxide model catalysts: Tailoring activity and stability by varying the Ti/Fe ratio. *Applied Catalysis A: General*, 533, 38-48. <https://doi.org/10.1016/j.apcata.2017.01.002>

**Important note**

To cite this publication, please use the final published version (if applicable).  
Please check the document version above.

**Copyright**

Other than for strictly personal use, it is not permitted to download, forward or distribute the text or part of it, without the consent of the author(s) and/or copyright holder(s), unless the work is under an open content license such as Creative Commons.

**Takedown policy**

Please contact us and provide details if you believe this document breaches copyrights.  
We will remove access to the work immediately and investigate your claim.

# High-Temperature Fischer-Tropsch Synthesis over FeTi mixed oxide model catalysts; Tailoring activity and stability by varying the Ti/Fe ratio

*Vera P. Santos<sup>†,‡,\*</sup>, Liam Borges<sup>†</sup>, Sina Sartipi<sup>†</sup>, Bart van der Linden<sup>†</sup>, A. Iulian Dugulan<sup>‡</sup>, Adam Chojecki<sup>‡</sup>, Thomas Davidian<sup>§</sup>, Matthijs Ruitenbeek<sup>§</sup>, Garry R. Meima<sup>‡,§</sup>, Freek Kapteijn<sup>†</sup>, Michiel Makkee<sup>†</sup> and Jorge Gascon<sup>†,\*</sup>*

*<sup>†</sup>Catalysis Engineering, Chemical Engineering Department, University of Technology, Van der Maasweg 9, 2629 HZ Delft, The Netherlands,*

*<sup>‡</sup>Applied Sciences, Fundamental Aspects of Materials and Energy, Delft University of Technology, Van der Maasweg 9, 2629 HZ Delft, The Netherlands,*

*<sup>§</sup>Core R&D, <sup>§</sup>Hydrocarbons R&D, Dow Benelux B.V., P.O. Box 48, 4530 AA, Terneuzen, The Netherlands*

## Abstract

A series of Fe-Ti mixed oxide model catalysts containing different Ti/Fe ratios were synthesized and applied as catalysts for the High Temperature Fischer-Tropsch reaction (HTFTS). XRD, H<sub>2</sub>-TPR and *in situ* Mössbauer and XAFS spectroscopy were applied to evaluate the role of Ti on the physical and chemical properties of Fe within the mixed metal oxide. It was observed that the Ti/Fe ratio determines the relative amounts of *hematite*, *pseudobrookite*, and *anatase* in the starting materials. The interplay between these phases is responsible for the HTFTS catalytic performance.

Our results demonstrate that the presence of *pseudobrookite*: i) enhances the dispersion of iron; ii) mediates and controls the reduction and carburization degree during the transformation of Fe (III) species to carbides upon activation, and iii) increases the stability under HTFTS conditions by minimizing the re-oxidation of iron carbides. Highest catalytic activity and stability is achieved for the material with Ti/Fe ratio of 1/2.1.

## 1. Introduction

Depletion of oil sources and the need to reduce the carbon footprint have directed extensive research efforts into the development of alternative feedstocks and processes to produce chemicals. [1-3] Among these, High Temperature Fischer-Tropsch Synthesis (HTFTS) is a promising alternative technology for the production of short chain olefins from natural gas, coal or biomass. [4-7] This process converts syngas, a mixture of hydrogen and carbon monoxide, to hydrocarbons on a iron catalyst. [8, 9] The product distribution from an HTFTS process follows the Anderson-Schulz-Flory (ASF) distribution, making it theoretically impossible to selectively synthesize a narrow product distribution. According to this theoretical model, the maximum selectivity of C<sub>2</sub>-C<sub>4</sub> hydrocarbons (including olefins and paraffins) is 58% and is achieved with a chain growth probability (alpha value) between 0.4 and 0.5. [6]

One of the most efficient ways of shifting product selectivity to low carbon numbers (low alpha) is by increasing the reaction temperature. However, a decrease of the chain growth probability also results in an undesired increase of methane selectivity as predicted by the ASF distribution. In addition, catalyst deactivation accelerates at higher temperatures. These aspects have been considered to be the major restrictions for the industrial application of this process. [10, 11]

Fe-based catalysts remain the practical catalyst choice for the HTFTS process. [8, 12, 13] Fe-based catalysts produce less methane and more olefins than Co-based catalysts at high conversion levels (conversion higher than 20%). Furthermore, they are active in the water-gas-shift reaction under typical HTFTS conditions, enabling the *in situ* re-adjustment of the H<sub>2</sub>/CO molar ratio for the conversion of hydrogen lean syngas. [8]

Extensive research has been carried out to improve the activity and selectivity towards short chain olefins in iron-based catalysts while minimizing the formation of methane and mitigating deactivation phenomena. Between mid 1970 and mid 1980 Ruhrchemie (now Johnson Matthey) developed different catalysts for the HTFTS process by mixing iron oxide with oxides of other metals such as Ti,

V, Mo, W or Mn. [14, 15] Comparable systems were reported by The Dow Chemical Company in the same period. [16] In particular, an important model system composed of bulk iron oxide promoted with titanium, zinc, and potassium oxide was developed for industrial applications. [17] These catalytic systems showed high selectivity towards lower olefins while exhibiting a low methane make (10%) and serve as the reference in bulk HTFTS catalyst development. [17] However, the effect of each catalytic component on the HTFTS performance and their promoting mechanism are still poorly understood.

In a recent work, the phase composition of a Fe-Ti-Zn-K-oxide reference catalyst was studied in the early stages of the HTFTS reaction with *operando* spectroscopy tools. [18] However, this work did not systematically probe the parameters that might affect such transformations. In the current work we therefore focus on simple model systems based on iron-titanium mixed oxides, i.e. without the use of additional promoters like alkali, etc. The purpose of this study is to unravel the role of the Fe-Ti interactions on the HTFTS catalyst performance and stability, by the use of different *in situ* characterization techniques in combination with catalyst performance testing.

## 2. Materials and Methods

### 2.1 Synthesis

A series of iron-titanium mixed oxides with different Ti/Fe ratios ( $0.1 < \text{Ti/Fe} < 2.6$ ) were synthesized as follows: 10 ml of a saturated solution of oxalic acid, an aqueous solution of iron(III) nitrate nonahydrate (2.0 mol/L), and a solution of titanium(IV) bis(ammonium lactato) dihydroxide (50 wt. %) were mixed under vigorous orbital shaking (500 rpm, RT) in such proportions to achieve the Ti/Fe atomic ratio (1/10 – 3/7 – 5/5 – 7/3). Subsequently, the final mixture was heated to 363 K (5 K/min; continuous orbital shaking) and held at that temperature for up to 16 h to evaporate the excess of water resulting in a gel-like residue. Finally, the residue was calcined under static oven conditions (ramp 5 K/min; T = 723 K, hold time 4 h).

## 2.2 Characterization

### 2.2.1 X-ray fluorescence (XRF)

X-ray Fluorescence (XRF) data were collected at room temperature (RT) with a PANalytical PW4400 spectrometer using an X-ray tube with a rhodium anode.

### 2.2.2 X-ray Diffraction

X-ray diffraction (XRD) patterns were recorded in a Bragg–Brentano geometry in a Bruker D8 Advance diffractometer equipped with a Vantec position sensitive detector and graphite monochromator. Measurements were performed at room temperature, using monochromatic Cu  $K\alpha$  radiation ( $\lambda = 1.5406 \text{ \AA}$ ) in the  $2\theta$  region between  $10^\circ$  and  $90^\circ$ . Samples were placed on a Si (5 1 0) substrate and rotated during measurements. All patterns were background-subtracted to eliminate the contribution of air scatter and possible fluorescence radiation.

### 2.2.3 *In situ* Mössbauer spectroscopy

Transmission  $^{57}\text{Fe}$  Mössbauer spectra were collected at 300 and 4.2 K with constant and sinusoidal velocity spectrometers using a  $^{57}\text{Co}(\text{Rh})$  source. Velocity calibration was carried out at room temperature, using an  $\alpha$ -Fe foil. The source and the absorbing samples were kept at the same temperature during the measurements. The low-temperature Mössbauer measurements were performed in a cryostat in which the in-situ cell was fully immersed in liquid helium. The temperatures of both source and sample were continuously monitored using Cryogenic Linear Temperature Sensors (CLTS). The Mössbauer spectra were fitted using the Mösswinn 4.0 program.

The experiments were performed in a state-of-the-art high-pressure Mössbauer *in situ* cell – recently developed at TU Delft. [19] The Mössbauer spectrometer is operated in a vertical configuration – allowing the use of powders inside the sample chamber of the in-situ cell. The catalysts were used in the as-received state, without any additional sample handling. The high-pressure beryllium windows used in this cell contain 0.08% Fe impurity whose spectral contribution was fitted and removed from the final spectra. *In situ* reduction experiments were performed under hydrogen atmosphere at 698 K,

3 bar. A spectrum was recorded after 3 h exposure. *In situ* syngas conversion experiments were carried at 20 bar, 613 K, and H<sub>2</sub>/CO ratio of 1. A spectrum was recorded after 5 h exposure.

#### **2.2.4 Temperature Programmed Reduction (H<sub>2</sub>-TPR)**

Temperature-programmed reduction (TPR) was used to evaluate the reducibility of Fe on the different catalysts used. These experiments were performed using hydrogen as reducing agent.

In a typical experiment, 50-130 mg of sample was placed in a fixed bed reactor and exposed to a mixture of 10% H<sub>2</sub>/He, and heated using a rate of 10 K /min from RT to 1100 K with a flow-rate of 20 cm<sup>3</sup>/min (STP). The outlet composition of the gas mixture was measured as a function of time, using a thermal conductivity detector (TCD) and mass spectrometer (MS).

The extent of reduction ( $\zeta$ ) was calculated from the integral consumption of hydrogen within the temperature range of TPR experiment assuming that Fe is in the final reduced form.

#### **2.2.5 *In situ* X-ray Absorption spectroscopy**

X-Ray absorption spectroscopy was performed at beamline X18A of National Synchrotron Light Source in Brookhaven National Laboratory (NY, USA). The beamline used the Si (1 1 1) channel-cut monochromator and provided an energy range of 5–25 keV. All the measurements were performed in transmittance mode. Incident and transmitted X-rays were detected with ion chambers. EXAFS and XANES data were collected on the K edge of Fe. All Fe-containing samples were measured against the Fe-foil used as a reference.

In a typical *in situ* experiment, the samples were diluted with boron nitrate to achieve a desired edge jump value. Subsequently, the sample was placed in an *in situ* cell, and was continuously purged with a flow of He of 20 cm<sup>3</sup>/min (STP) and heating was applied. Once the sample reached 723 K, XAS spectra were collected until no further changes were observed. For the reduction step the cell was cooled to 673 K and exposed to a flow of H<sub>2</sub>/He (1:9). The flow rate was 20 cm<sup>3</sup>/min (STP) and the cell pressure was 2 bar. The reduction process was monitored by EXAFS/XANES for 3 hours. When

no further evolution of the spectra was apparent the reduction was discontinued and the reduced catalyst was exposed to Fischer-Tropsch (FTS) conditions. FTS reaction was carried out at 613 K in a flow of CO/H<sub>2</sub> (1:1) mixture at the flow rate of 60 cm<sup>3</sup>/min (STP).

The EXAFS data were processed in Athena software package (version 0.8.056). The background subtraction was performed by using the automated single-variable fit implemented in Athena. The Fourier Transform of the reciprocal space data was performed by using the Hanning window in the  $k$  range of 2–10 Å<sup>-1</sup>.

### **2.2.6 Transmission Electron Microscopy**

High-resolution transmission electron micrographs were collected on a JEOL model JEM-2010 working at 200 kV with a LaB<sub>6</sub> filament. It reaches a resolution between layers of 0.14 nm and between points of 0.25 nm. The microscope is equipped with an Orius 831 camera from Gatan. A suspension in ethanol was made and grinded with a mortar and pestle. The suspension is further dispersed in an ultrasonic bath for 5 min. A drop of that suspension is deposited onto an Au grid covered with carbon and left to dry in air.

### **2.3 HTFTS Catalytic testing**

HTFTS experiments were performed in a 48 parallel-flow fixed-bed micro-reactor setup. [20] In order to avoid condensation of products, an inert gas flow (N<sub>2</sub>) was injected downstream to the reactor at the same reactor temperature to dilute the product streams.

For all experiments, ~10 mg of fresh catalyst with a particle size of 177–420 μm was diluted with 100 μL SiC particles of the same size. Samples were firstly activated *in situ* by pure H<sub>2</sub> at 698 K for 3 h at 3 bar followed by cooling to 613 K under H<sub>2</sub> flow at the same pressure. After increasing the pressure to the process value (20 bar), a 5 cm<sup>3</sup> min<sup>-1</sup> flow (STP) consisting of CO 45 vol. %, H<sub>2</sub> 45 vol. % and He 10 vol. % was introduced. A rate of 2 K min<sup>-1</sup> was applied for all the heating/cooling steps.

A Siemens Maxum Process GC, equipped with multiple columns and detectors in parallel, analyzed permanent gases as well as hydrocarbon products up to C<sub>6</sub> in the gas phase online.

CO conversion ( $X$ , %), carbon selectivity ( $S_{C_n}$ %) and molar fraction ( $y$ , -) of each product were defined by equations (1), (2), and (3), respectively, where  $X$  stands for CO conversion,  $F$  indicates the molar flow rate,  $S$  is the carbons selectivity towards a product with  $n$  carbon atoms and  $y$  is the molar fraction of a hydrocarbon  $C_n$ . The molar flows were calculated using helium as internal standard (relative standard deviation 5%).

$$X = \frac{F_{in,CO} - F_{out,CO}}{F_{CO,in}} \times 100 \quad \text{Eq. (1)}$$

$$S_{C_n} = \frac{nF_{C_n}}{F_{CO_2} + \sum_{n=1}^N nF_{C_n}} \times 100 \quad \text{Eq. (2)}$$

$$y_{C_n} = \frac{F_{C_n}}{\sum_{n=1}^N F_{C_n}}, N = 6 \quad \text{Eq. (3)}$$

Catalytic activity is expressed as iron-time-yield (FTY), defined as the number of CO moles converted to hydrocarbons per gram of Fe per second.

$$FTY = \frac{XF_{in,CO}}{w_{Fe}} \times 100 \quad \text{Eq. (4)}$$

where  $S_{CO_2}$  is the selectivity towards  $CO_2$ ,  $w_{Fe}$  the mass of Fe in the catalyst sample,  $M_{Fe}$  the molar mass of Fe.

### 3. Results

A series of Fe-Ti mixed oxide catalysts with different Ti/Fe molar ratio were synthesized and evaluated in the HTFTS reaction. The materials are denominated as  $Fe_xTi_y$  where  $x$  and  $y$  represent the elemental composition of Fe and Ti, respectively, determined by XRF (Table 1). The chemical composition determined by XRF is in agreement with the intended Ti/Fe atomic ratios.

#### 3.1 Structural, coordination and morphological properties of Fe on fresh mixed oxides

The long range order of iron and titanium was determined by X-ray diffraction (XRD). Figure 1a shows the diffraction patterns for the mixed oxides and reference compounds, namely *hematite* ( $\alpha$ - $Fe_2O_3$ ) and *anatase*. The quantification of each crystalline phase was obtained by whole pattern fitting procedure (the Easy-Quant module of the Jade 9.5 software package) and the results are summarized

in Table 1. The detailed description of these analyses can be found in the supporting information (SI, Figure S1).

The Ti/Fe ratio determines the crystalline phase composition of the resulting mixed oxide.  $Fe_{0.7}Ti$  was composed by *hematite* (89 wt. %) and *anatase* (11 wt. %). A closer investigation of the diffraction lines corresponding to the (101) plane of  $\alpha$ - $Fe_2O_3$  (Figure 1b) demonstrates a shift towards lower angles in comparison to the pure reference,  $\alpha$ - $Fe_2O_3$ , which indicates an expansion of the crystal lattice. However, considering the sizes of both cations (0.64 Å for  $Fe^{3+}$  and 0.61 Å for  $Ti^{4+}$  for octahedral coordination), a contraction of the lattice would be expected if Ti(IV) replaces Fe(III) sites. The lower overall density of the material may be an indication of the presence of Schottky defects. These defects are generally formed upon doping, and consist of a vacant cation lattice site and a vacant anion lattice site. To form a Schottky defect, ions leave their normal lattice positions and relocate at the crystal surface, preserving overall charge neutrality. [20] When the Ti/Fe molar ratio increased from 0.1 to ~ 0.5, the relative amount of *hematite* decreased from 89 wt. % to 53 wt.%, while the *anatase* phase increased from 11 wt.% to 34 wt. %. In addition, new diffraction lines at 21.06, 29.77, 38.00, 54.06, and 70 ° $2\theta$  emerged, indicating the formation of a new crystalline phase, *i.e. pseudobrookite* ( $Fe_2TiO_5$ , JCPDS File No. 41-1432). The percentage of *pseudobrookite* in  $Fe_{2.1}Ti$  is ~13 wt. %, and is in the form of very small crystalline domains according to the XRD patterns. With an increase of the Ti/Fe molar ratio from ~ 0.5 to 1 the relative amount of *pseudobrookite* increased significantly from 13 wt.% to 35 wt.% at the expense of the hematite phase. In  $FeTi_{2.6}$ , XRD fitting analyses suggest that all iron is in the form of *pseudobrookite*. ~~It should be noted, however, that the Ti/Fe determined by XRD is slightly higher when compared to XRF (see Table 1), which may indicate that there are amorphous or highly dispersed phases rich in iron that are not detected by XRD.~~

The coordination and valence state of iron were evaluated by Mössbauer and XAFS. The Mössbauer spectra of fresh samples determined at 4.2 K are shown in Figure 2, and the parameters derived from the analysis of these spectra are summarized in Table 2. The combination of isomer shift and quadrupole splitting were in agreement with the presence of Fe(III) in octahedral coordination. [21] Furthermore, the iron atoms within the mixed oxide are distributed in 2 different phases: *hematite* and

*pseudobrookite*, in agreement with XRD analysis. At room temperature (see Supporting Information Figure S2, Table S1), hematite is characterized by a sextet, while *pseudobrookite* (together with dispersed *hematite* structures) exhibits doublets. [22] At 4.2 K, the two components are fully separated and can be analyzed individually on the basis of their specific hyperfine yields (Table 2). The relative amounts of *pseudobrookite* detected by Mössbauer are higher when compared with the XRD analyses, which may indicate that part of this phase is in amorphous state or in highly dispersed form.

The grain size of the magnetic (bulk) *hematite* structures was estimated using the Mössbauer spectra determined at 300 K (see Supporting Information, Figure S2 and Table S1), using the relationship between the magnetic hyperfine field of ferromagnetic particles and the particle volume. [21, 23, 24] The incorporation of Ti improves the dispersion of *hematite* within the mixed oxide; for example, the particle size of *hematite* is ~ 45 nm for Fe<sub>8.7</sub>Ti while for FeTi is 33 nm (Table S2).

Figure 3 shows the normalized XANES spectra at RT. The XANES spectra of the fresh samples are characterized by a pre-edge peak at ~ 7113.0 eV corresponding to the forbidden  $1s \rightarrow 3d$  transition, and the main edge peak ( $1s \rightarrow 4p$ ) at around 7123 eV, characteristic of the presence of Fe (III) species. [12, 25, 26] The absorption edge energy of Fe<sub>2.1</sub>Ti, FeTi and FeTi<sub>2.6</sub> is slightly higher than those of Fe<sub>8.7</sub>Ti and  $\alpha$ -Fe<sub>2</sub>O<sub>3</sub>, mostly because of the presence of an Fe-O-Ti structure with an electronic inductive effect between Fe(III) and Ti(IV) species. Furthermore, the pre-edge peak intensity was significantly higher than that of the reference compound  $\alpha$ -Fe<sub>2</sub>O<sub>3</sub>, and increased in the following order: FeTi<sub>8.7</sub> < Fe<sub>2.1</sub>Ti < FeTi  $\approx$  FeTi<sub>2.6</sub>. This observation indicates that Fe(III) species in the mixed oxides with a high Ti/Fe ratio exhibit the most severe structure distortion. [27-29]

The morphological features were characterized by HR-TEM. Figures 4 and 5 show the HR-TEM images of Fe-Ti mixed oxides. Regardless of the Ti/Fe ratio, all samples displayed three distinct morphologies which were associated with a different chemical composition: 1) particles with irregular form and broad size distribution (20-50 nm diameters, Figure 4b). EDX analysis may suggest that these particles correspond to the *hematite* phase, since they are rich in Fe; 2) spherical particles with diameter ranging from 3-10 nm (Figure 4c), which are rich in Ti; the measured lattice distance in the

fringes was found to be 0.35 nm which corresponds well with the (101) plane of *anatase*; 3) spherical-like particles below 10 nm which are easily aggregated as floccules (Figure 4 d). These aggregates are developed in close contact with the *hematite* phase as can be seen in Figure 4d.

The relative amounts of each morphologic feature as well as the degree of interaction between these phases are a function of the Ti/Fe ratio. More specifically, the overall morphology of  $\text{Fe}_{8.7}\text{Ti}$  and  $\text{Fe}_{2.1}\text{Ti}$  is very similar due to the very low Ti/Fe ratio (see Figure 5a and 5b). In both cases, the irregular particles are the dominant features (1); some inter-crossed lattice fringes are also observed, suggesting higher crystallinity. In contrast, in  $\text{FeTi}$  and  $\text{FeTi}_{2.6}$  these features are less frequent due to the higher Ti/Fe ratio and the material is more homogeneous. Overall, the observed particle size decreases with Ti/Fe ratio, in agreement with Mössbauer spectroscopy (see Table S1).

The nitrogen adsorption-desorption isotherms are illustrated in Figure S3. For  $\text{FeTi}_{2.6}$ , the isotherm resembles closely with type IV (IUPAC classification), which is typical for mesoporous materials (pore size between 2 and 50 nm). The hysteresis is characterized by a plateau at high  $P/P_0$  and by parallel adsorption/desorption branches due to adsorption in unconnected mesopores with a relatively narrow pore size distribution. With the decrease of Ti/Fe ratio, from 2.6 to 0.1, the isotherms in the high  $P/P_0$  range shifted from a type IV to a type II pattern. This indicates the formation of macropores, which was probably caused by the aggregation of oxide particles in these samples.

Upon decreasing Ti/Fe ratio, the hysteresis loop also shifted from H1 type (low  $P/P_0$ ) to H3 type (high  $P/P_0$ ). Hysteresis type H3 is due to non-rigid pore structures which can be between individual particles. The external surface areas of the fresh catalysts were determined from nitrogen physisorption data using the t-method and are represented in Table S2. The external surface area increases from 37 to 53  $\text{m}^2/\text{g}$ , when the Ti/Fe ration increases from 0.1 to 2.6.

### **3.2 Reducibility and Phase transformations of Fe-Ti mixed oxides upon $\text{H}_2$ exposure**

The reducibility of Fe was evaluated by  $\text{H}_2$ -TPR, *in situ* Mössbauer spectroscopy and *in situ* XANES. Figure 6a shows the  $\text{H}_2$ -TPR profiles for Fe-Ti mixed oxides and reference *hematite*. The TPR- $\text{H}_2$  of *anatase* was also performed and did not show reduction peaks in the temperature range of the

experiment. Therefore, the assumption can be made that all reduction peaks can be assigned to reduction of iron species. The reducibility is expressed as hydrogen consumed normalized by the iron loading ( $\chi$ ). Table 3 summarizes the temperature of the first reduction peak as well as the H<sub>2</sub>/Fe molar ratio for the selected temperature ranges.

The reduction pattern of reference *hematite* ( $\alpha$ -Fe<sub>2</sub>O<sub>3</sub>) is characterized by a sharp peak centered at 675 K and two overlapping peaks centered at  $\sim$  929 and 1000 K, in agreement with previous studies. [21, 30] The mechanism of reduction of *hematite* is well described in the literature and it is characterized by a two-stage reduction process, wherein *magnetite* (Fe<sub>3</sub>O<sub>4</sub>) and *wüstite* (FeO) are the intermediate reduced species. Based on hydrogen consumption (see Table 3), the first peak in the TPR pattern was assigned to the reduction of  $\alpha$ -Fe<sub>2</sub>O<sub>3</sub> to Fe<sub>3</sub>O<sub>4</sub> (degree of reduction  $\sim$  97 %) while at higher temperatures these species are further converted to FeO and metallic iron (Fe<sup>0</sup>). The overall degree of reduction (temperature range 273-1100 K) calculated from the integral hydrogen consumption and considering Fe<sup>0</sup> as the final reduced state, is  $\sim$  75 % for  $\alpha$ -Fe<sub>2</sub>O<sub>3</sub> (Table 3).

The H<sub>2</sub>-TPR profile of the various materials is also shown in Figure 6a. The shape of these curves depends strongly on the composition of the material (Ti/Fe molar ratio). The reduction patterns of Fe<sub>8.7</sub>Ti and Fe<sub>2.1</sub>Ti, are very similar to the reference material ( $\alpha$ -Fe<sub>2</sub>O<sub>3</sub>) but all peaks are slightly shifted to lower temperatures. In addition, the hydrogen consumption (Table 3; atomic H<sub>2</sub> to Fe ratio  $\sim$  0.17) associated to the first onset of reduction is very similar in all samples. In terms of overall degree of reduction ( $\xi$ ) (Figure 6b), it decreases from 67 % to 58 % when the Ti/Fe ratio varies from 0 to 0.47. Further incorporation of Ti increases the complexity of the reduction profile. The TPR patterns of FeTi and FeTi<sub>2.6</sub> consist of several overlapping peaks in which the low temperature peak is shifted to higher temperatures in comparison with the reference  $\alpha$ -Fe<sub>2</sub>O<sub>3</sub>. The overall degree of reduction was only 34 % that was significantly lower than measured for  $\alpha$ -Fe<sub>2</sub>O<sub>3</sub>.

*In situ* Mössbauer spectroscopy was also carried out to unravel the type of iron species formed during reduction. The corresponding Mössbauer parameters calculated from the spectra are presented in Table 4 and Figure S4. Four iron species were identified after reduction, *viz.* a zero valent (metallic) iron species, two divalent iron species and one trivalent iron species. The trivalent species are assigned to

$\text{Fe}_2\text{TiO}_5$ , while Fe(II) species could neither be fitted to FeO nor to  $\text{Fe}_3\text{O}_4$ . Most probably these species arise from the reduction of  $\text{Fe}_2\text{TiO}_5$  to partially reduced titanates (*i.e.* *ulvöspinel* or *ilmenite*). The reduction degree, directly expressed as the relative amount of metallic iron present on the sample, decreases significantly with the Ti/Fe ratio, in agreement with TPR analysis. For example, reduced  $\text{Fe}_{8.7}\text{Ti}$  is mostly composed of  $\text{Fe}^0$ , while reduced  $\text{Fe}_{2.1}\text{Ti}$  is composed of 74 %  $\text{Fe}^0$ , 5 %  $\text{Fe}_2\text{TiO}_5$  and 21 % Fe(II). Further increase in Ti/Fe ratio inhibits significantly the formation of metallic iron from 74 to 23 %.

The observations from  $\text{H}_2$ -TPR and *in situ* Mössbauer spectroscopy studies were further supported by *in situ* XANES. Figure 6c shows the XANES spectra after reduction under hydrogen atmosphere. Upon exposure to  $\text{H}_2$  the Fe (III) species are reduced, as observed by the shift of the edge position from 7123 to 7121 eV, which is consistent with the presence of Fe(II) species. [12, 28]

### **3.3 Structural transformations on $\text{H}_2$ pre-treated catalysts during Fischer-Tropsch synthesis**

The composition of the different materials during Fischer Tropsch synthesis was investigated by *in situ* Mössbauer spectroscopy and is shown in Table 5 and Figure S4.  $\text{Fe}^0$  was not present in any of the samples, indicating that the major part of this phase was consumed during HTFTS and transformed into carbides and/or reduced oxides. Under syngas reaction conditions and after 5 h of time on stream,  $\epsilon'$ - $\text{Fe}_{2.2}\text{C}$  and  $\text{Fe}_5\text{C}_2$  are the major carbides encountered together with iron oxide species. The relative amount of each component after 5h syngas conversion was a function of the Ti/Fe ratio. For example, the relative amount of iron atoms in the form of carbides ( $\epsilon'$ - $\text{Fe}_{2.2}\text{C}$  and  $\chi$ - $\text{Fe}_5\text{C}_2$ ) decrease in the following order:  $\text{Fe}_{2.1}\text{Ti}$  (93%) >  $\text{Fe}_{8.7}\text{Ti}$  (85%) >  $\text{FeTi}$  (32%) ~  $\text{FeTi}_{2.6}$  (32%).

The relative amount of  $\text{Fe}_2\text{TiO}_5$  after reduction and syngas treatment did not change significantly during the considered time on stream, demonstrating that this phase was rather stable and did not transform into carbides or  $\text{Fe}^0$ . More importantly, the susceptibility of other phases to oxidation under FTS conditions was found to depend on the Ti/Fe ratio. For example, for  $\text{Fe}_{8.7}\text{Ti}$  there is re-oxidation

of iron carbide species into Fe(III), while this effect was not observed on the samples with higher Ti/Fe ratios, such as Fe<sub>2.1</sub>Ti.

### 3.4 HTFTS Catalytic performance

The conversion profiles ( $X$ , %) of the different catalysts are presented in Figure 7a. In all cases an initial transient period of about 15 hours was observed, wherein the catalytic activity decreased with time-on-stream (“lining down”). During this period, the “apparent” deactivation rate correlated with the Ti/Fe ratio: FeTi<sub>2.6</sub> < FeTi < Fe<sub>2.1</sub>Ti < Fe<sub>8.7</sub>Ti. After this period, the conversion levels over FeTi and FeTi<sub>2.6</sub> remained fairly unchanged, while Fe<sub>8.7</sub>Ti continued to slowly deactivate. In contrast, the conversion over Fe<sub>2.1</sub>Ti increased over time. Since these catalysts contained different iron loadings, the catalytic activity is expressed as iron time yield, defined as the moles of CO converted to hydrocarbons per second and per gram of iron. Figure 7b shows that Fe<sub>2.1</sub>Ti is the most promising composition because of its relatively high intrinsic catalytic activity with FTY that is 1.5 times higher than those calculated for the other catalysts.

The product distribution of all materials does obey the Anderson-Schulz-Flory (ASF) distribution regime. The calculated chain growth probability ( $\alpha$ ) decreased from 0.5 to 0.4 upon increasing the Ti/Fe ratio from 0.1 to 2.6 (Figure S5 and Table S3). Accordingly, methane selectivity was the highest for the catalysts containing higher Ti loading (FeTi and FeTi<sub>2.6</sub>), albeit the conversion levels were significantly lower than those for Fe<sub>8.7</sub>Ti and Fe<sub>2.1</sub>Ti. The C2-C3 olefin fraction in C2-C3 hydrocarbons product did not change significantly with the Ti/Fe ratio (approximately 0.3 for all studied cases (Table 6)).

Taking in consideration the catalytic activity and product distribution (selectivity towards methane and selectivity towards olefins) Fe<sub>2.1</sub>Ti is the most interesting catalytic system of this study.

## 4. Discussion

Mixed metal oxides have been widely investigated due to their interesting catalytic properties. The addition of an auxiliary element to the matrix of a pure metal oxide or the formation of solid solutions can greatly modify the structural, redox and catalytic properties of the resulting solid.

XRD and Mössbauer spectroscopy demonstrated that the overall composition and coordination of iron varies with the Ti/Fe ratio. Accordingly, Fe can be in two different environments, *i.e.* in the form of  $\text{Fe}_2\text{TiO}_5$  or  $\alpha\text{-Fe}_2\text{O}_3$ . For  $\text{Ti/Fe} < 0.1$  ratio, *hematite* and *anatase* are the only phases observed. For  $0.46 < \text{Ti/Fe} < 2.6$ , a triphasic system, composed of *pseudobrookite*, *anatase*, and *hematite* is observed. *Pseudobrookite* is a mixed oxide that is formed with migration of  $\text{Ti}^{4+}$  into the *hematite* structure [19]. This occurs because the ionic radii for  $\text{Ti}^{4+}$  and  $\text{Fe}^{3+}$  are very similar (*vide supra*) leading to a metal-site disorder, in which  $\text{Ti}^{4+}$  and  $\text{Fe}^{3+}$  positions cannot be crystallographically distinguished.

The structural disorder upon incorporation of Ti is also confirmed by XANES, by studying the pre-edge features of Fe K edge. The XANES of FeTi oxides shows that the intensity of the pre-edge peak increases significantly from pure iron oxide ( $\alpha\text{-Fe}_2\text{O}_3$ ) to highly titania loaded mixed oxide ( $\text{FeTi}_{2.6}$ ). The increase in intensity of the  $1s \rightarrow 3d$  dipolar forbidden transition indicated that the iron center lost the centro-symmetry which could be a result of the change in the coordination (transition from octahedral to tetrahedral) and/or the mixing of  $3d$  and  $4p$  orbitals caused by structural distortion. [27-29, 31] Accordingly, we can deduce that the interaction between iron and titanium species leads to a structure distortion from six fold coordination in  $\alpha\text{-Fe}_2\text{O}_3$  to a five-fold or four-fold coordination in the Fe-Ti mixed oxide.

These structural and electronic changes are found to significantly affect the redox properties and carburization degree of iron within the mixed oxide. The results discussed so far demonstrate an inverse relationship between the amount of *pseudobrookite* and the overall reduction degree (Figure 6b), and this behaviour can be explained by the kinetics of reduction of *pseudobrookite*. The reduction mechanism of  $\text{Fe}_2\text{TiO}_5$  has been well described in literature and may involve multiple intermediates such as *ilmenite* ( $\text{FeTiO}_3$ ), *ferro-pseudobrookite* ( $\text{FeTi}_2\text{O}_5$ ), and *ulvöspinel* ( $\text{Fe}_2\text{TiO}_4$ ) depending on the process conditions. Majority of studies identify *ilmenite* as the key intermediate product of the *pseudobrookite* reduction process. [32] This phase transition can occur at temperatures lower than 773 K depending on the lability of oxygen and the interaction between Fe and Ti. The further reduction of *ilmenite* to metallic iron generates titania and occurs at much higher temperatures than the reduction of

$\text{Fe}_3\text{O}_4$  ( $T > 920 \text{ K}$ ). Rates of reduction are generally 50 to 200 times lower than that of *pseudobrookite* and, therefore, *ilmenite* stabilizes the Fe(II) species by acting as an Fe(II) sink.

Mössbauer spectroscopy showed that the reducibility of *pseudobrookite* varies with the Ti/Fe ratio. For example, in  $\text{Fe}_{2.1}\text{Ti}$ , 80 % of the atoms present in the form of  $\text{Fe}_2\text{TiO}_5$  were reduced to Fe(II), and all these species were further converted into carbides upon exposure to syngas. In contrast, in FeTi only 45 % of the atoms present in the form of  $\text{Fe}_2\text{TiO}_5$  were reduced to Fe(II), and these species were hardly transformed into carbides during syngas conversion. We speculate that the intimate contact between these phases induces geometric and electronic effects, thereby, influencing the redox behavior of *pseudobrookite*.

The redox and carburization degrees correlate well with the observed HTFTS activities. For example, Figure 9b demonstrates that  $\text{Fe}_{2.1}\text{Ti}$  is the optimal composition to achieve the highest activity since this material shows the highest carburization degree (93 %). In contrast, FeTi and  $\text{FeTi}_{2.6}$  are much poorer catalysts since only 30 % of the iron atoms can be transformed to Hägg carbides. These results are in agreement with previous literature studies that correlate the HTFTS performance with the relative degree of reduction and carburization. [33-35] Carbide formation over metallic iron is more kinetically favoured when compared with reduced iron oxides, due to higher rate of bulk diffusion of carbon [36, 37].

~~For example, Steynberg *et al.* [35] demonstrated that there is a corrat least 60 % of reduction of iron into  $\text{Fe}^0$  is needed to achieve maximum activity, since  $\text{Fe}^0$  rapidly dissolves carbon into its crystal lattice forming the desired iron carbides.~~

The Ti/Fe ratio is also found to govern the deactivation rates. Although  $\text{Fe}_{2.1}\text{Ti}$  and  $\text{Fe}_{8.7}\text{Ti}$  show similar conversion levels during the first 10 hours on stream, the deactivation rate for  $\text{Fe}_{8.7}\text{Ti}$  is very pronounced. The observed deactivation may be a result of an interplay between various mechanisms including the oxidation of carbides, sintering, and carbon deposition. [12] In terms of re-oxidation of carbide phase during syngas conversion, Mössbauer spectroscopy shows a correlation between susceptibility to oxidation and the Ti/Fe ratio, in particular on the amount of *pseudobrookite*. *Pseudobrookite* moderates the redox character of Fe and avoids re-oxidation during syngas

conversion. Moreover, the presence of this solid solution may affect the growth of carbide phases by preventing its agglomeration (i.e., structural spacer). Liu *et al.* describes similar phenomena when iron is doped with manganese [38] Furthermore, the spatial restriction created by the presence of titania and *pseudobrookite* may minimize the nucleation of carbon deposits and, as such, slow down deactivation. [6, 13].

## 4. Conclusions

A series of Fe-Ti mixed oxides containing different Ti/Fe ratios were synthesized and applied as catalysts for the HTFTS reaction. Structural analyses demonstrate that the Ti/Fe ratio determines the crystal composition of the final solid, more specifically the relative amounts of *anatase*, *hematite*, and *pseudobrookite*.

The characterization results demonstrated that *pseudobrookite* suppressed the crystal domain growth and mediates the reduction and carburization degree of iron. An appropriate amount of *pseudobrookite* (*pseudobrookite* < 13 wt.%) enhanced the carburization degree and minimized the re-oxidation of carbides during syngas conversion, therefore improving the HTFTS performance. Among all FeTi oxides, Fe<sub>2.1</sub>Ti is the optimal composition for High Temperature Fischer Tropsch applications.

## Acknowledgments

The authors acknowledge financial support from The Dow Chemical Company. We acknowledge Gerard Bonte for operating the Fischer-Tropsch reactors.

## References

- [1] T. Ren, M. Patel, K. Blok, *Energy*, 31 (2006) 425.
- [2] L. Chiari, A. Zecca, *Energy Policy*, 39 (2011) 5026.
- [3] D.A. Wood, *Journal of Natural Gas Science and Engineering*, 26 (2015).
- [4] M.E. Dry, *J. Mol. Catal.*, 17 (1982) 133.
- [5] R. Snel, *Catal. Rev.*, 29 (1987) 361.
- [6] H.M. Torres Galvis, K.P. de Jong, *ACS Catal.*, 3 (2013) 2130.
- [7] M. Janardanarao, *Ind. Eng. Chem. Res.*, 29 (1990) 1735.
- [8] S. Abelló, D. Montané, *ChemSusChem*, 4 (2011) 1538.
- [9] B. Sun, K. Xu, L. Nguyen, M. Qiao, F. Tao, *ChemCatChem*, 4 (2012) 1498.
- [10] S.A. Eliason, C.H. Bartholomew, *Appl. Catal., A*, 186 (1999).
- [11] Y. Zhang, N. Sirimanothan, R.J. O'Brien, B.H. Davis, H.H. Hamdeh, Study of Deactivation of Iron-Based Fischer-Tropsch Synthesis Catalysts, in: G.W.R. J.J. Spivey, B.H. Davis (Eds.) *Studies in Surface Science and Catalysis*, Elsevier, 2001, pp. 125-132.
- [12] E. de Smit, B.M. Weckhuysen, *Chem. Soc. Rev.*, 37 (2008) 2758.
- [13] H.M. Torres Galvis, J.H. Bitter, C.B. Khare, M. Ruitenbeek, A.I. Dugulan, K.P. de Jong, *Science*, 335 (2012) 835.
- [14] B.D.C.D. Buessemeier, D.C.D.F.C. Dieter, G.D.C.D. Horn, W.D.C.D. Kluy, DE 2536488 B1, 1976.

- [15] C.B. Murchison, D.A. Murdick, US 4199522 A, 1980.
- [16] C.H. Murchison, R.L. Weiss, R.A. Stowe, *J. Chem. Educ.*, 63 (1986) 213.
- [17] B. Bussemeier, C.D. Frohning, G. Horn, W. Kluy, US 4564642 A, 1986.
- [18] I.D. Gonzalez-Jimenez, K. Cats, T. Davidian, M. Ruitenbeek, F. Meirer, Y. Liu, J. Nelson, J.C. Andrews, P. Pianetta, F.M.F. de Groot, B.M. Weckhuysen, *Angew. Chem. Int. Ed.*, 51 (2012) 11986.
- [19] V.P. Santos, T.A. Wezendonk, J.J.D. Jaén, A.I. Dugulan, M.A. Nasalevich, H.-U. Islam, A. Chojecki, S. Sartipi, X. Sun, A.A. Hakeem, A.C.J. Koeken, M. Ruitenbeek, T. Davidian, G.R. Meima, G. Sankar, F. Kapteijn, M. Makkee, J. Gascon, *Nat Commun*, 6 (2015) 1.
- [20] S. Hirokazu, mark McAdon, Rick Shroden, Garry Meima, Adam Chojecki, Peter Catry, Billy bardin, *Heterogeneous Catalysis High Throughput Workflow: A Case Study Involving Propane Oxidative Dehydrogenation*, 2014.
- [21] E. Kuzmann, S. Nagy, A. Vértes, Critical review of analytical applications of Mössbauer spectroscopy illustrated by mineralogical and geological examples (IUPAC Technical Report), in: *Pure and Applied Chemistry*, 2003, pp. 801.
- [22] R.G. Teller, M.R. Antonio, A.E. Grau, M. Gueguin, E. Kostiner, *J. Solid State Chem.*, 88 (1990) 334.
- [23] F. Bødker, S. Mørup, *Europhys. Lett.*, 52 (2000) 217.
- [24] H. Dlamini, T. Motjope, G. Joorst, G. ter Stege, M. Mdleleni, *Catal. Letters*, 78 (2002) 201.
- [25] M.C. Ribeiro, G. Jacobs, B.H. Davis, D.C. Cronauer, A.J. Kropf, C.L. Marshall, *J. Phys. Chem. C*, 114 (2010) 7895.
- [26] F. Liu, K. Asakura, P. Xie, J. Wang, H. He, *Catal. Today*, 201 (2013) 131.
- [27] F. Liu, H. He, C. Zhang, Z. Feng, L. Zheng, Y. Xie, T. Hu, *Applied Catalysis B: Environmental*, 96 (2010) 408.
- [28] F. Liu, H. He, Y. Ding, C. Zhang, *Applied Catalysis B: Environmental*, 93 (2009) 194.
- [29] F. Liu, K. Asakura, H. He, Y. Liu, W. Shan, X. Shi, C. Zhang, *Catal. Today*, 164 (2011) 520.
- [30] D.H. Chun, J.C. Park, S.Y. Hong, J.T. Lim, C.S. Kim, H.-T. Lee, J.-I. Yang, S. Hong, H. Jung, *J. Catal.*, 317 (2014) 135.
- [31] F. Liu, H. He, L. Xie, *ChemCatChem*, 5 (2013) 3760.
- [32] S. Jørstad, *Reduction of Pelletized Tyssedal Ilmenite and the Effect of Changing Gas Composition and Flow, Pellet Size and Pre Oxidation Condition*, in, Norwegian University of Science and Technology Department of Materials Science and Engineering, Trondheim, 2011.
- [33] M.C. Ribeiro, G. Jacobs, R. Pendyala, B.H. Davis, D.C. Cronauer, A.J. Kropf, C.L. Marshall, *J. Phys. Chem. C*, 115 (2011) 4783.
- [34] B.H. Davis, *Catal. Today*, 141 (2009) 25.
- [35] A.P. Steynberg, R.L. Espinoza, B. Jager, A.C. Vosloo, *Appl. Catal., A*, 186 (1999) 41.
- [36] E. de Smit, F. Cinquini, A.M. Beale, O.V. Safonova, W. van Beek, P. Sautet, B.M. Weckhuysen, *Journal of the American Chemical Society*, 132 (2010) 14928.
- [37] J.W. Niemantsverdriet, A.M. van der Kraan, *J. Catal.*, 72 (1981).
- [38] T. Li, Y. Yang, C. Zhang, X. An, H. Wan, Z. Tao, H. Xiang, Y. Li, F. Yi, B. Xu, *Fuel*, 86 (2007) 921.

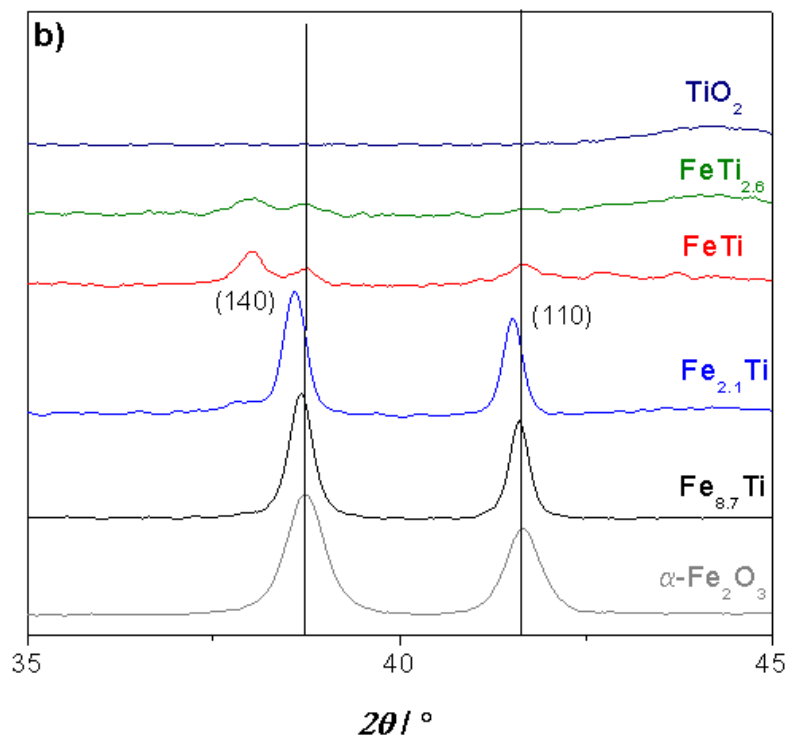
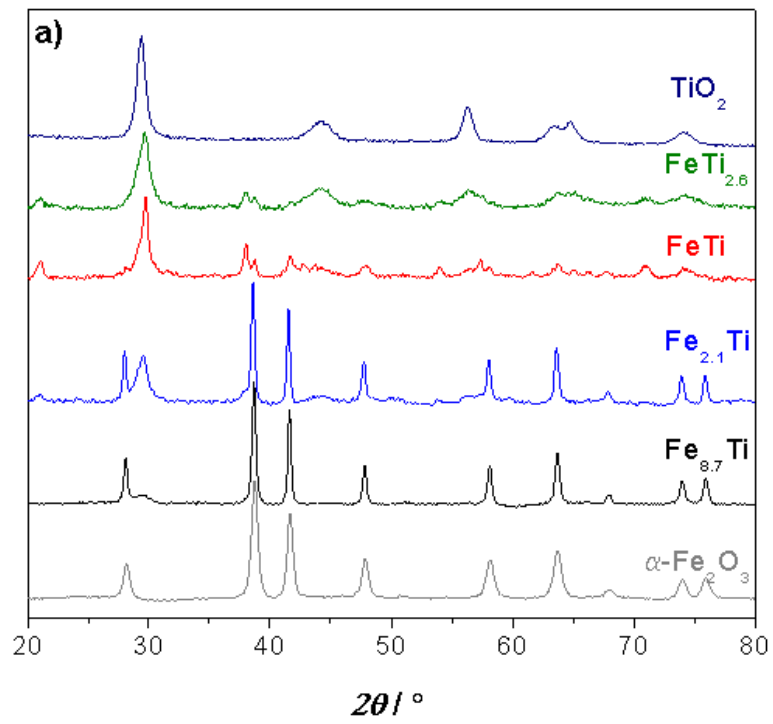
## Figures

# High-Temperature Fischer-Tropsch Synthesis over FeTi mixed oxide model catalysts; Tailoring activity and stability by varying the Ti/Fe ratio

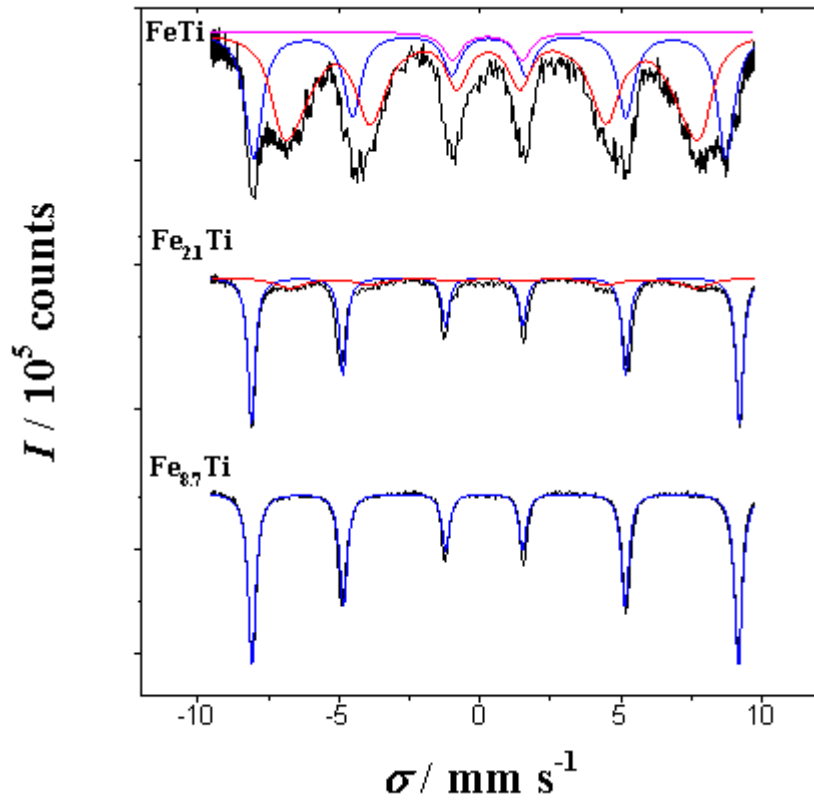
*Vera P. Santos<sup>†,‡,\*</sup>, Liam Borges<sup>†</sup>, Sina Sartipi<sup>†</sup>, Bart van der Linden<sup>†</sup>, A. Iulian Dugulan, Adam Chojecki<sup>‡</sup>, Thomas Davidian<sup>§</sup>, Matthijs Ruitenbeek<sup>§</sup>, Garry R. Meima<sup>‡,§</sup>, Freek Kapteijn<sup>†</sup>, Michiel Makkee<sup>†</sup> and Jorge Gascon<sup>†,\*</sup>*

*<sup>†</sup>Catalysis Engineering, Chemical Engineering Department, <sup>‡</sup>Applied Sciences, Fundamental Aspects of Materials and Energy, Delft University of Technology, Van der Maasweg 9, 2629 HZ Delft, The Netherlands,*

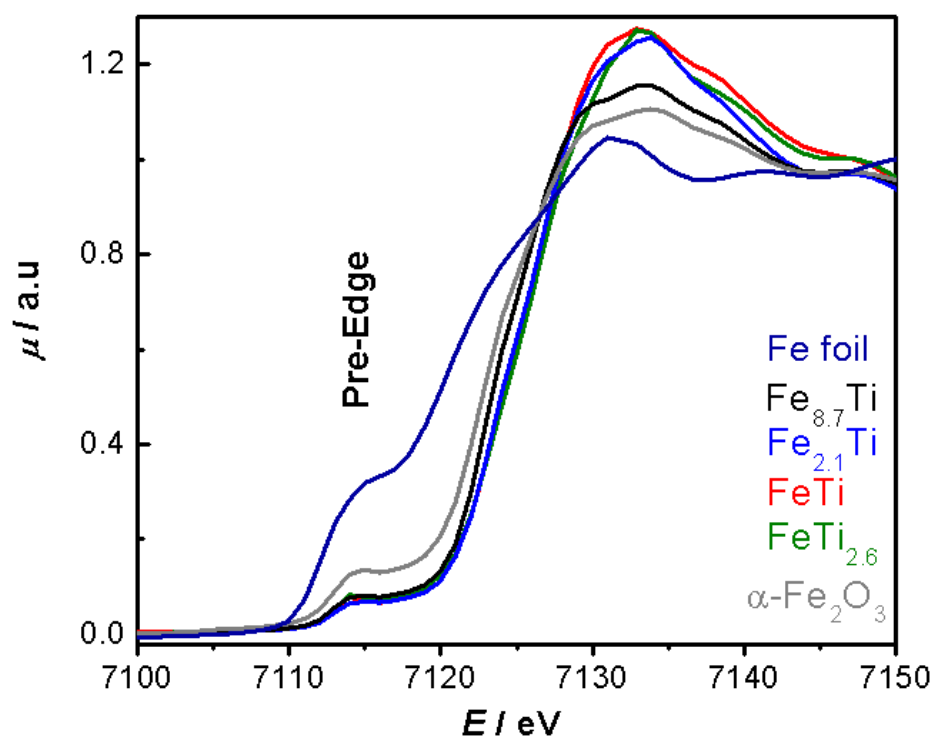
*<sup>‡</sup>Core R&D, <sup>§</sup>Hydrocarbons R&D, Dow Benelux B.V., P.O. Box 48, 4530 AA, Terneuzen, The Netherlands*



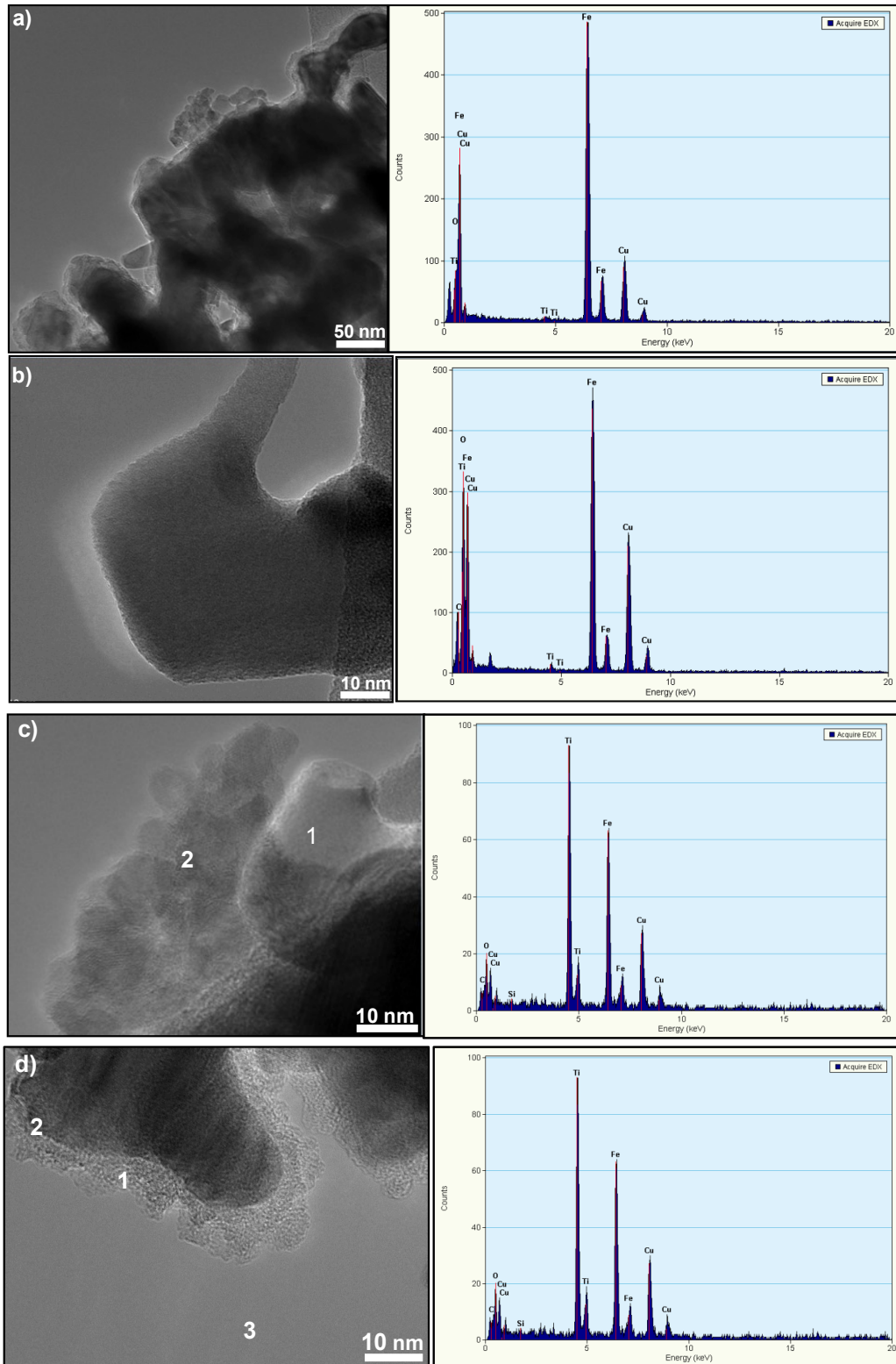
**Figure 1.** a) XRD powder diffraction patterns of iron titanium mixed oxides and reference materials (anatase and hematite); b) Magnification of diffraction peaks correspondent to the (101) plane of hematite.



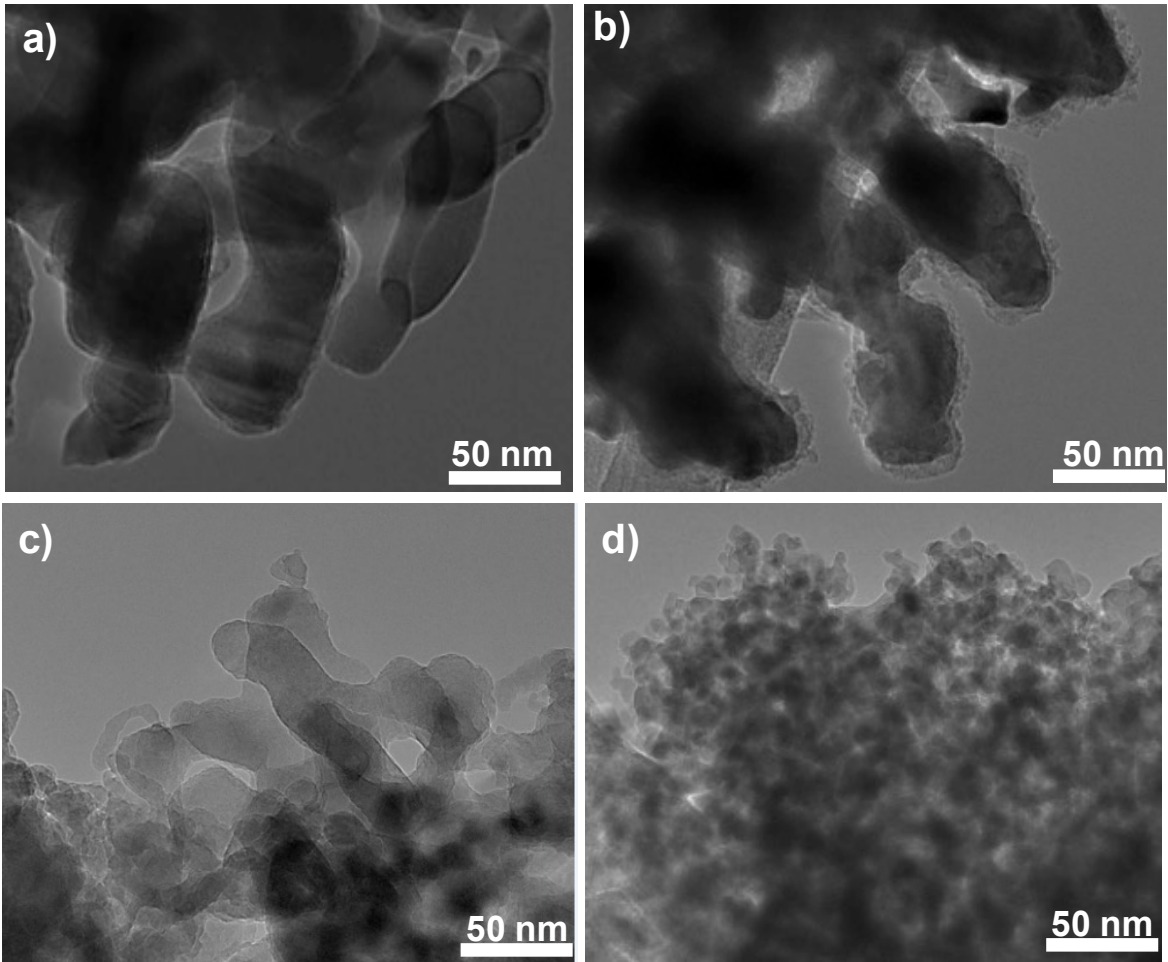
**Figure 2.** Mössbauer spectra of fresh Fe-Ti mixed oxides obtained at 4.2 K.



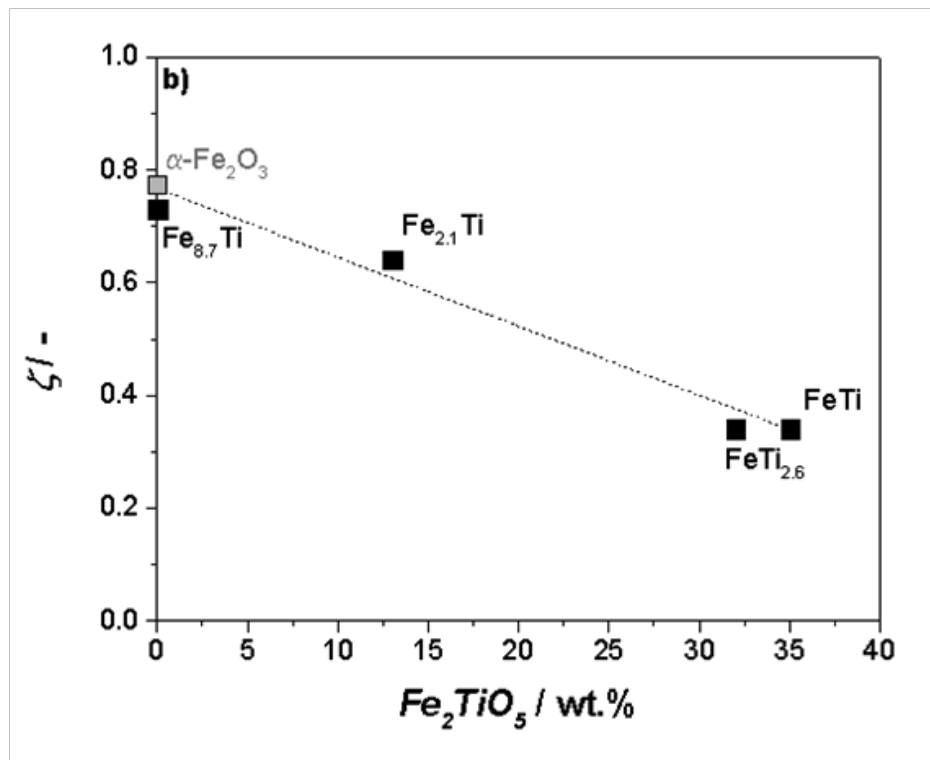
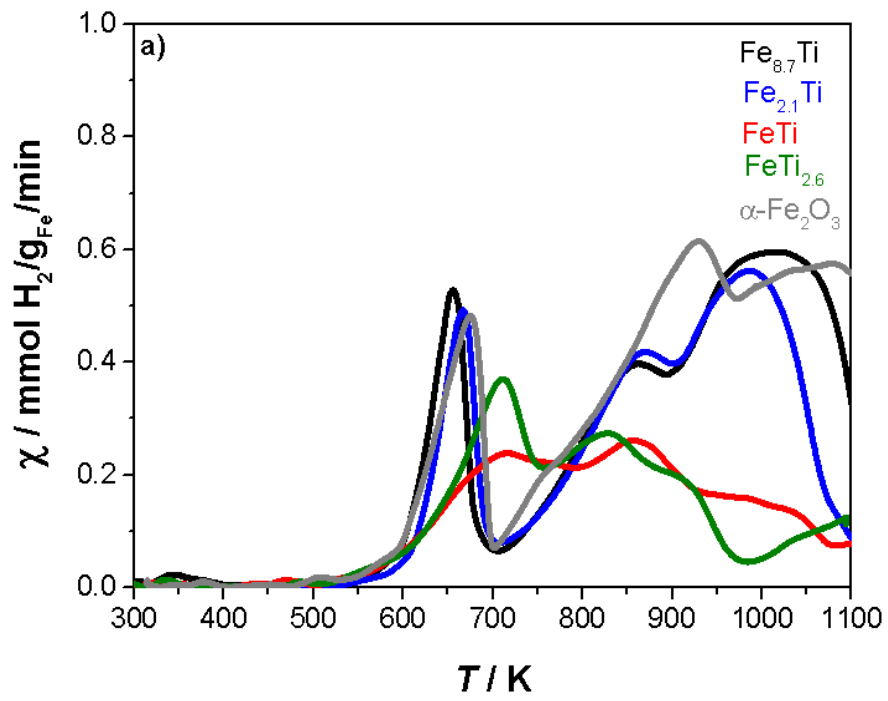
**Figure 3.** XANES of  $Fe_xTi_y$  and reference materials (Fe foil and  $\alpha$ -Fe<sub>2</sub>O<sub>3</sub>) recorded at room temperature, wherein  $\mu$  represents the normalized absorption.



**Figure 4.** a) TEM micrograph and EDX analysis on fresh  $\text{Fe}_{8.7}\text{Ti}$ ; b) TEM micrograph of  $\text{Fe}_{8.7}\text{Ti}$  on selected region rich on Fe; c) TEM micrograph of  $\text{Fe}_{8.7}\text{Ti}$  on selected region richer on Ti; d) TEM micrograph on  $\text{Fe}_{2.1}\text{Ti}$  on selected region highlighting the 3 different morphologies detected on  $\text{Fe}_x\text{Ti}_y$ .



**Figure 5.** HR-TEM micrographs of  $\text{Fe}_x\text{Ti}_y$  a)  $\text{Fe}_{8.7}\text{Ti}$ ; b)  $\text{Fe}_{2.1}\text{Ti}$ ; c)  $\text{FeTi}$ ; d)  $\text{FeTi}_{2.6}$ .



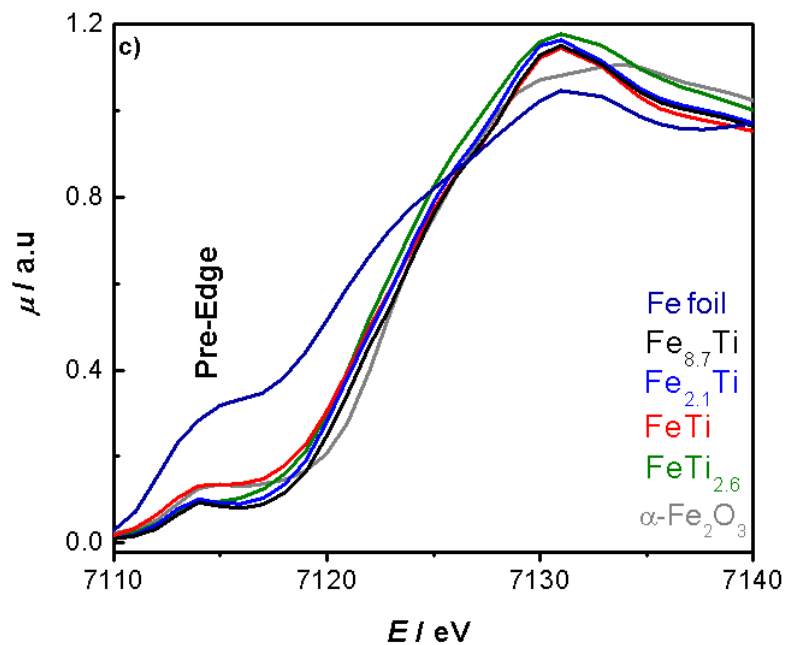


**Figure 6** a) TPR profiles of Fe-Ti mixed oxides and reference material ( $\alpha$ -Fe<sub>2</sub>O<sub>3</sub>).  $\chi$  represents the hydrogen consumption per gram of iron ( $\text{mmol g}_{\text{Fe}}^{-1} \text{min}^{-1}$ ); b) Effect of pseudobrookite fraction determined by XRD (wt.%) on the overall degree of reduction ( $\zeta$ ) calculated from the integral consumption of hydrogen in the temperature range 200-1100 K; c) XANES spectra of Fe-Ti mixed oxides and corresponding reference materials ( $\alpha$ -Fe<sub>2</sub>O<sub>3</sub> and Fe foil) after reduction in H<sub>2</sub> at 698 K and 3 bar for 3 h.

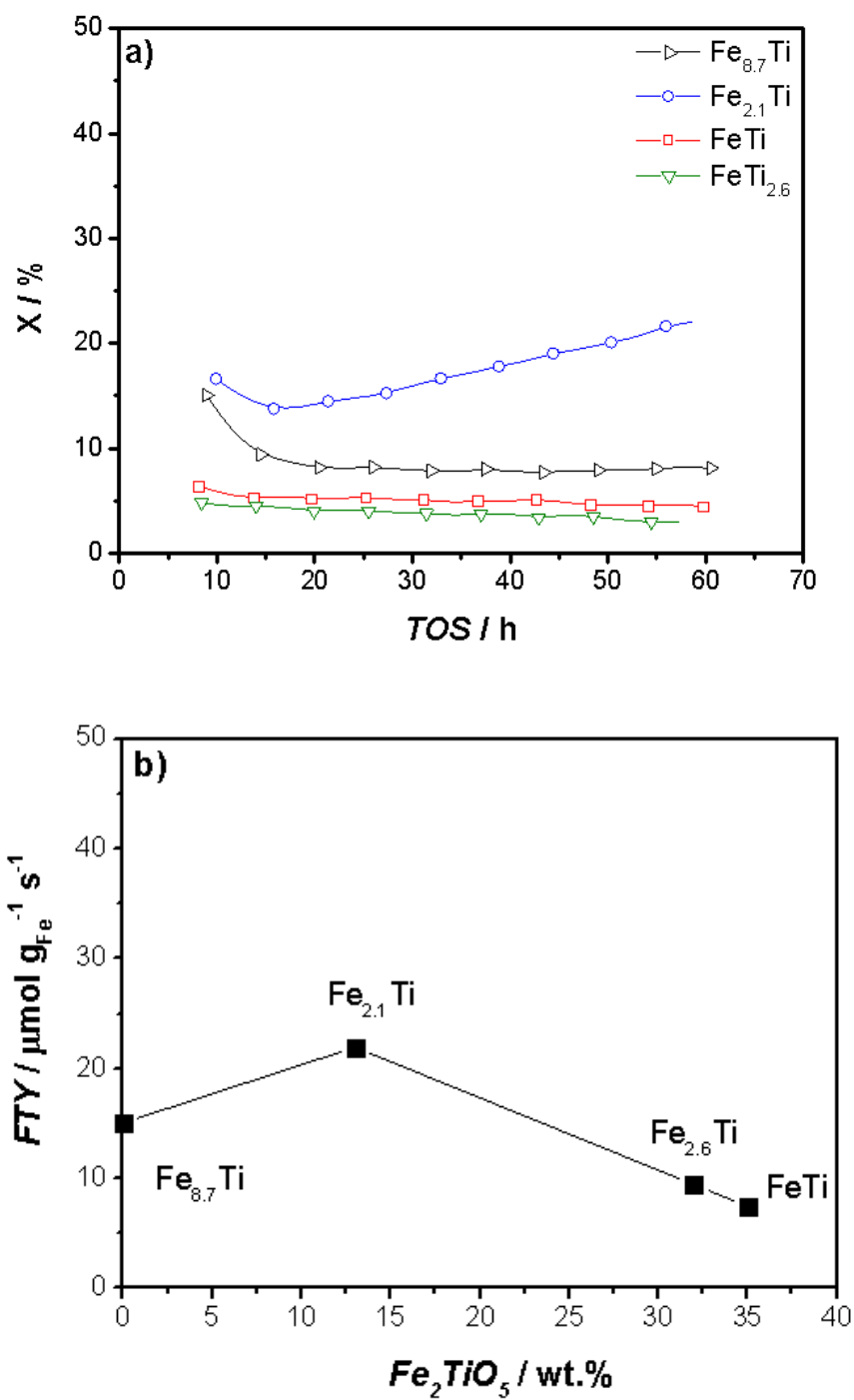


**Figure 7** a) CO conversion (X) versus time-on-stream (TOS) for un-promoted Fe-Ti mixed oxides. b) Iron time yield (FTY) after 80 h time on stream (TOS) as a function of the amount of pseudobrookite determined by XRD (Fe<sub>2</sub>TiO<sub>5</sub>). FTS conditions: 20 bar, 613 K and H<sub>2</sub> /CO= 1.